IEEE Access
Multidisciplinary | Rapid Review | Open Access Journal

Received May 19, 2021, accepted May 25, 2021, date of publication May 31, 2021, date of current version June 10, 2021.

Digital Object Identifier 10.1109/ACCESS.2021.3085083

Assessment of Predictive Current Control of Six-Phase Induction Motor With Different Winding Configurations

ABDULLAH SHAWIER[1], ABDELRAHMAN HABIB[1], MOHAMED MAMDOUH[2], AYMAN SAMY ABDEL-KHALIK[1], (Senior Member, IEEE), AND KHALED H. AHMED[3], (Senior Member, IEEE)

[1]Department of Electrical Engineering, Alexandria University, Alexandria 21544, Egypt
[2]Department of Electrical Power and Machines, Tanta University, Tanta 31527, Egypt
[3]Department of Electronic and Electrical Engineering, Strathclyde University, Glasgow G1 1XQ, U.K.

Corresponding author: Abdullah Shawier (es-abdallh.shawier@alexu.edu.eg)

ABSTRACT Asymmetrical six-phase (A6P) induction motor-based drives can be considered as a well-established employed technology in high-power safety-critical industry sectors. Of the different control techniques proposed for multiphase machines, model predictive control (MPC) has recently been favored thanks to its simplicity, rapid dynamic response, and flexibility to define new control objectives. One of the main operating challenges when employing MPC to A6P induction machine is the poor quality of the phase current waveform due to the relatively low impedance of the secondary xy subspace. Although different controller structures have been introduced in the available literature to mitigate this problem, most of the available proposals, if not affecting the dc-link voltage utilization, will likely add to the control complexity. From the stator winding layout perspective, this paper attempts to investigate the effect of different winding configurations of six-phase stators with isolated neutral arrangements on the performance of predictive current control (PCC). This study shows that the winding configuration affect the mapping of the 64 available voltage vectors to the $\alpha\beta$ and xy subspaces, the induced current ripples, and the required weighting factor employed in PCC. The theoretical findings have experimentally been validated using a 1kW twelve-phase machine that can externally be reconnected to form any of the three available six-phase winding configurations.

INDEX TERMS Six-phase, dual three-phase, asymmetrical, symmetrical, predictive current control, voltage space decomposing.

I. INTRODUCTION

Multi-phase induction machines have long attracted both industry and academia especially in high-power safety-critical applications [1], [2]. That was motivated by the simultaneous need for high performance drive systems along with stringent levels of reliability. The most up-to-date research in this field is still showing a persistent interest to highlight the various benefits of this promising technology in various industrial applications such as automotive, aerospace, ship propulsion, and offshore wind energy generation systems [2]. Consequently, recent literature has discussed several challenges such as control, machine design,[3], [4] parameter identifications [5], fault detection and post-fault operation [6], [7] as well as some other innovative applications [8], [9].

As a matter of fact, increasing the phase order not only enhances the machine degrees of freedom and post-fault reliability, but also reduces the per phase ratings, which in turn alleviates the required power semiconductors ratings [10]. However, the complexity and cost of the power inverter will also dramatically increase, which practically limits the available choices in many applications to certain phase orders. On one hand, literature has extensively covered machines with prime phase orders such as five and seven phase machines [2], [11]. On the other hand, machines with multiple three-phase winding have been practically dominating since the readily commercial three-phase off-the-shelf

The associate editor coordinating the review of this manuscript and approving it for publication was Kan Liu.

power converters as well as available control techniques can still be recruited [12]. In the same context, the standard three-phase machines can simply be used to construct these machines without technical constraints.

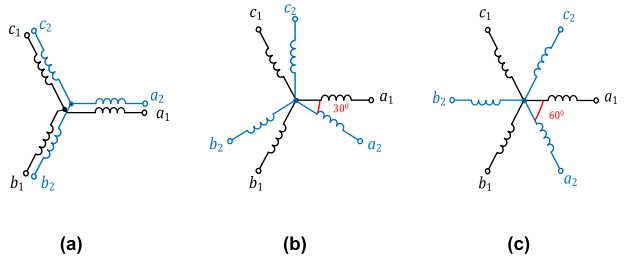

FIGURE 1. Different configurations of six-phase winding. (a) D3P. (b) A6P. (c) S6P.

As a result, various configurations of six-phase induction machine (SPIM) has been proposed in literature consisting of two three-phase winding sets with an arbitrary spatial phase shift angle between the two sets [13], [14]. Based on the winding arrangement, six-phase machine could be classified into dual three-phase (D3P), asymmetrical six-phase (A6P), and symmetrical six-phase (S6P) machines with a spatial phase angle between the two-winding sets of 0°, 30°, and 60°, respectively, as shown in Fig. 1. Among these available three options, it is fair to say that the A6P is the most deployed configuration in most industrial applications [15]. Historically, this choice was motivated by the absence of the fifth and seventh flux harmonics in the A6P stators, which eliminates the sixth order torque ripple component. Besides, A6P is the only six-phase winding layout with the capability of torque density enhancement using third order harmonic current injection [16]. However, it has been proven that with an appropriate choice of the switching frequency, the harmonic contents and, thus, the developed torque for the three configurations may fairly be comparable [17], [18]. The recent study introduced in [13] has compared the parameters and performance of three equivalent six-phase machines having same dimensions and copper volumes with the three possible winding configurations (D3P, A6P, and S6P). This has been carried out using a 12-phase machine with a double layer winding and a 5/6 coil span. This recommended chorded winding design is commonly employed in practical six-phase stators. The terminals of the 12 phases are externally reconfigured to form any of the three six-phase winding configurations, as detailed in [13]. The study showed the following interesting conclusions:

- The fundamental sequence circuit parameters are the same for both D3P and S6P, while the A6P shows a slightly higher leakage inductance, which slightly affects the maximum machine pullout torque.
- The equivalent leakage inductance of the secondary subspace is much lower for the A6P than D3P and S6P connections. That was basically the main reason behind the experienced intolerable circulating *xy* currents when A6P connection is used.
- The D3P corresponds to minimum zero sequence impedance, which is highly favored to maximize the dc-link utilization of the stator winding under post-fault operation with connected neutrals.
- The D3P generally outperforms the three connections in terms of efficiency and current quality.

Based on these conclusions, it was stimulating to extend the effect of winding layout on the performance of recent controllers that are highly dependent on the machine parameters, which has not been conceived so far.

As far as the control of multiphase machine is concentered, using voltage space decomposition (VSD) modeling approach [19] has been recognized to facilitate the extension of the well-established control methods like field oriented control (FOC) and direct torque control (DTC) for multi-phase machines [20]. However, it is found to be more complicated compared to standard three-phase controllers due to the existence of the circulating currents of the secondary (xy) subspace. Thus, extra current control loops have to be added in order to regulate these disrupting current components and reduce stator harmonic current distortion [21]. Moreover, sophisticated modulation techniques should be utilized as proposed in [22] for A6P and in [23], [24] for S6P machines.

Recently, model predictive control (MPC) has successfully proven itself as a promising alternative to classical controllers for different power converters [25] due to its simplicity and ease of handling nonlinearities and constrains. In particular, finite control set MPC (FCS-MPC) is the most convenient algorithm to undertake the discrete nature of power converter while avoiding the modulation stage in other controllers. These salient merits motivate the implementation of predictive current control (PCC) in multi-phase machines in recent studies [26]–[29]. Nevertheless, there are some well-known problems associated with the implementation of FCS-MPC such as the variable switching frequency, the weighting factor design, and the computational burden [30]. Consequently, many solutions have been proposed to overcome these challenges for FCS-MPC based multi-phase drives. In order to reduce the computational burden, a reduced number of voltage vectors (VV) out of the admissible 64 VVs has been used for the A6P configuration [29]. The optimization stage of the PCC algorithm of six-phase machines should deal with both the ($\alpha\beta$) and (xy) subspaces. Thus, an appropriate weighting factor should carefully be design [31]. In [32], a weighting factor elimination technique is proposed using modified prediction model and cost function based on the double dq modelling technique. A novel solution is also presented in [33] based on the concept of virtual voltage vectors (VVV). This method greatly minimizes the effect of the circulating currents, while simplifying the design and implementation of FCS-MPC. However, it results in a higher switching frequency, while it reduces the DC link voltage utilization. In [34], an FCS-MPC with a lower complexity has been introduced using a predefined lookup table to eliminate the useless VVVs, which has, in turn, relatively reduced the

computational burden. The problem of variable switching frequency was also addressed in [35], where constant switching frequency was achieved by utilizing a combination of zero vectors and selected VVVs during each control sample.

The mitigation of the high circulating (xy) currents in six-phase induction machines has also been dealt with in the recent literature using some special winding configurations [36], [37], which offer a high secondary subspace inductance and can successfully suppress the effect of the circulating current without complicating the control design.

Although most of the conducted research in MPC of six-phase motors was mainly focusing on the A6P configuration, a recent study introduced in [38] has investigated the application of an integrated S6P motor in electric vehicles using predictive torque control (PTC) for both charging and propulsion modes of operation. To the best of the authors' knowledge, application of FCS-MPC to D3P motors has not been addressed so far. Moreover, most available proposals assume that ensuring zero xy voltage component of the applied VV will guarantee zero current component, which represents also a rather idealistic assumption. Experimental investigations have proven that xy current components at fundamental frequency or even order harmonics may take place due to machine/inverter asymmetries, which has not also been highlighted so far. This paper, therefore, aims to investigate the effect of winding configuration of SPIM on the performance of conventional PCC. The presented study covers the effect of winding configuration on phase current ripple, subspaces voltage vectors, dc-link utilization, weighting factor effect, and dynamic response. In order to achieve a fair comparison, same stator with the same copper volume and dimensions has been used for all winding configurations. The theoretical findings have experimentally been validated using a 1 kW twelve-phase machine that can externally be reconnected to form any of the three different windings of SPIM [13]. The current study is limited to healthy case with isolated neutrals arrangement, which is the preferably employed neutral arrangement under healthy conditions.

The mathematical VSD based model for a general SPIM is first given in Section II. The VVs mapping among the $\alpha\beta$ and xy subspaces as well as the effect of winding/inverter asymmetry on the induced circulating current components are also explained in the same section. Based on the conclusions made, Section III further discusses the implementation of PCC using different winding configurations and their suitable voltage vectors to suppress the circulating xy current components due to either applied VVs and/or winding asymmetry. The experimental results are then introduced in Section IV, while the paper is concluded in Section V.

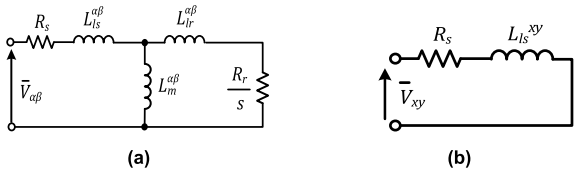

FIGURE 2. Equivalent circuits of SPIM. (a) $\alpha\beta$. (b) xy subspaces.

II. MACHINE AND INVERTER MODELING

This section discusses the modelling of six-phase machines based on classical voltage space decomposition (VSD). Although it has been shown in [13] that the winding layout will affect the equivalent parameters of the sequence circuits, the sequence circuits shown in Fig. 2 will be the same for all winding configurations. This section also investigates the inverter modelling under isolated neutrals arrangement (2N) as well as the voltage vectors mapping among the $\alpha\beta$ and xy subspaces for the three available winding configurations. Under 2N arrangement, the zero-sequence subspace is simply discarded in all analysis [13].

A. MATHEMATICAL MODELLING OF SPIM

For isolated 2N six-phase winding with a general arbitrary angle δ between the two winding sets, the Clarke's transformation given by (1), as shown at the bottom of the page, can be used to obtain two orthogonal subspaces (i.e. fundamental $\alpha\beta$ and secondary xy) based on the machine phase quantities (i.e., voltage, current, and linkage flux) [15]. The angle δ equals 0°, 30°, and 60° for the D3P, A6P, and S6P configurations, respectively.

While considering only the dominant harmonics for both active subspaces, the voltage and flux linkage equations for the ($\alpha\beta$) and (xy) subspaces can be expressed in space phasor

$$T_{VSD} = \frac{1}{\sqrt{3}} \times \begin{bmatrix} 1 & \cos\left(\frac{2\pi}{3}\right) & \cos\left(\frac{4\pi}{3}\right) & \cos\delta & \cos\left(\delta+\frac{2\pi}{3}\right) & \cos\left(\delta+\frac{4\pi}{3}\right) \\ 0 & \sin\left(\frac{2\pi}{3}\right) & \sin\left(\frac{4\pi}{3}\right) & \sin\delta & \sin\left(\delta+\frac{2\pi}{3}\right) & \sin\left(\delta+\frac{4\pi}{3}\right) \\ 1 & \cos\left(\frac{4\pi}{3}\right) & \cos\left(\frac{2\pi}{3}\right) & -\cos\delta & -\cos\left(\delta+\frac{2\pi}{3}\right) & -\cos\left(\delta+\frac{4\pi}{3}\right) \\ 0 & \sin\left(\frac{4\pi}{3}\right) & \sin\left(\frac{2\pi}{3}\right) & \sin\delta & \sin\left(\delta+\frac{2\pi}{3}\right) & \sin\left(\delta+\frac{4\pi}{3}\right) \end{bmatrix} \quad (1)$$

form as follows:

$$\bar{v}_{\alpha\beta s} = R_s.\bar{i}_{\alpha\beta s} + p\bar{\lambda}_{\alpha\beta s} \quad (2)$$

$$0 = R_r.\bar{i}_{\alpha\beta r} + p\bar{\lambda}_{\alpha\beta r} + j\omega_r.\bar{\lambda}_{\alpha\beta r} \quad (3)$$

$$\bar{\lambda}_{\alpha\beta s} = (L_{ls}^{\alpha\beta} + L_m^{\alpha\beta})\bar{i}_{\alpha\beta s} + L_m^{\alpha\beta}.\bar{i}_{\alpha\beta r} \quad (4)$$

$$\bar{\lambda}_{\alpha\beta r} = (L_{lr}^{\alpha\beta} + L_m^{\alpha\beta})\bar{i}_{\alpha\beta r} + L_m^{\alpha\beta}.\bar{i}_{\alpha\beta s} \quad (5)$$

$$\bar{v}_{xys} = R_s\bar{i}_{xys} + L_{ls}^{xy}p\bar{i}_{xys} \quad (6)$$

It has been proven in [13] that the winding configuration will highly affect the value of the sequence leakage inductance of the secondary subspace, L_{ls}^{xy}, being minimum under A6P configuration.

B. INVERTER MODELING

The phase voltages of a six-phase inverter with isolated neutrals can be represented in terms of inverter switching state pattern as follows:

$$\begin{bmatrix} V_{a1} \\ V_{b1} \\ V_{c1} \\ V_{a2} \\ V_{b2} \\ V_{c2} \end{bmatrix} = \frac{1}{3}V_{DC} \begin{bmatrix} 2 & -1 & -1 & 0 & 0 & 0 \\ -1 & 2 & -1 & 0 & 0 & 0 \\ -1 & -1 & 2 & 0 & 0 & 0 \\ 0 & 0 & 0 & 2 & -1 & -1 \\ 0 & 0 & 0 & -1 & 2 & -1 \\ 0 & 0 & 0 & -1 & -1 & 2 \end{bmatrix} S \quad (7)$$

$$S = [S_1\ S_2\ S_3\ S_4\ S_5\ S_6]^T \quad (8)$$

where, $S_n \in \{0, 1\}$ is the switching state of leg n. At $S_n = 1$, the upper switch of leg n is ON, while the lower switch will be ON in case of $S_n = 0$.

Applying the VSD transformation defined by (1), the subspaces voltages could be calculated using (9).

$$V_{\alpha\beta xy} = T_{VSD}.V_{a_1 \to c_2} \quad (9)$$

The transformation given by (9) results in 64 different voltage vectors mapped into both $\alpha\beta$ and xy subspaces simultaneously. The voltage vectors corresponding to zero subspaces are not considered in a 2N arrangement six-phase machines since the zero-subspace is nullified. The numbering of voltage vectors commonly corresponds to the decimal equivalent value of the switching state, i.e., VV number 25 is realized by applying the switching state S = 011001. Whereas, the vector length represents the percentage dc-link utilization. Since the VSD matrix depends on the arbitrary angle δ, it is expected that each winding configuration will correspond to voltage vectors with different magnitudes and angles.

For the D3P configuration ($\delta = 0°$), the 64 available voltage vectors are mapped into $\alpha\beta$ and xy subspaces, with 10 zero voltage vectors. According to vector magnitude, the voltage vectors are categorized into Large, Medium, Small, and Zero voltage vectors with corresponding magnitudes of 0.6667, 0.5774, 0.333, and zero, respectively, keeping in mind that there is a redundancy in the small and medium vector sets.

While, under the A6P configuration ($\delta = 30°$), the 64 switching states result in 49 distinct voltage vectors in both $\alpha\beta$ and xy subspaces, simultaneously, which are, in turn, categorized into Large (L), Medium Large (ML), Medium (M), Small (S), and Zero (Z) vectors, with corresponding magnitudes of 0.644, 0.4714, 0.333, 0.1725 and zero pu, respectively.

TABLE 1. Voltage vectors classification in $\alpha\beta$ subspace.

Vector set	D3P		A6P		S6P	
	No. VV	Mag (p.u.)	No. VV	Mag (p.u.)	No. VV	Mag (p.u.)
L	6	0.6667	12	0.6447	6	0.6667
ML	0	0	12	0.4714	0	0
M	12	0.5774	24	0.3333	12	0.5774
S	36	0.3333	12	0.1725	36	0.3333
Zero	10	0	4	0	10	0

TABLE 2. Voltage vectors mapping to different subspaces.

Winding config.		$\alpha\beta$ -Vectors	xy -Vectors
D3P	Z	[0,7,14,21,28,35,42,49,56,63]	[0,7,9,18,27,36,45,54,56,63]
	S	[1,2,3,4,5,6,8,10,12,15,16,17,20, 23,24,29,30,31,32,33,34,39,40,43 ,46,47,48,51,53,55,57,58,59,60, 61,62]	[1,2,3,4,5,6,8,11,13,15,16,19,22, 23,24,25,26,31,32,37,38,39,40, 41,44,47,48,50,52,55,57,58,59, 60,61,62]
	M	[11,13,19,22,25,26,37,38,41,44 ,50,52]	[10,12,17,20,29,30,33,34,43,46 ,51,53]
	L	[9,18,27,36,45,54]	[14,21,28,35,42,49]
A6P	Z	[0,7,56,63]	[0,7,56,63]
	S	[12,14,17,21,28,29,34,35,42,46 ,49,51]	[9,11,18,22,26,27,36,37,41,45 ,52,54]
	M	[1,2,3,4,5,6,8,15,16,23,24,31,32, 39,40,47,48,55,57,58,59,60,61, 62]	[1,2,3,4,5,6,8,15,16,23,24,31,32, 39,40,47,48,55,57,58,59,60,61, 62]
	ML	[10,13,19,20,25,30,33,38,43,44, 50,53]	[10,13,19,20,25,30,33,38,43,44, 50,53]
	L	[9,11,18,22,26,27,36,37,41,45, 52,54]	[12,14,17,21,28,29,34,35,42,46, 49,51]
S6P	Z	[0,7,12,17,29,34,46,51,56,63]	[0,7,11,22,26,37,41,52,56,63]
	S	[1,2,3,4,5,6,8,13,14,15,16,19,21, 23,24,25,28,31,32,35,38,39,40, 42,44,47,48,49,50,55,57,58,59, 60, 61,62]	[1,2,3,4,5,6,8,9,10,15,16,18,20, 23,24,27,30,31,32,33,36,39,40, 43,45,47,48,53,54,55,57,58,59, 60,61,62]
	M	[9,10,18,20,27,30,33,36,43,45, 53,54]	[13,14,19,21,25,28,35,38,42,44, 49,50]
	L	[11,22,26,37,41,52]	[12,17,29,34,46,51]

Under S6P configuration ($\delta = 60°$), the mapping of the available 64 vectors will be the same as the D3P case in terms of voltage vector magnitudes and the vectors numbers in each level. However, the mapping to xy subspace totally differs from the D3P case. Table 1 summarizes the classification of the voltage vectors for each configuration based on their magnitudes in the $\alpha\beta$ subspace. While, Table 2 shows all available VVs in both subspaces and how they are mapped to different subspaces, which can be differentiated using the colored numbers representing different VVs. It should be noted that Table 2 only illustrates how the same VV can be mapped with different magnitudes to different subspaces, keeping in mind that the VVs orientation also might differ [32], [37].

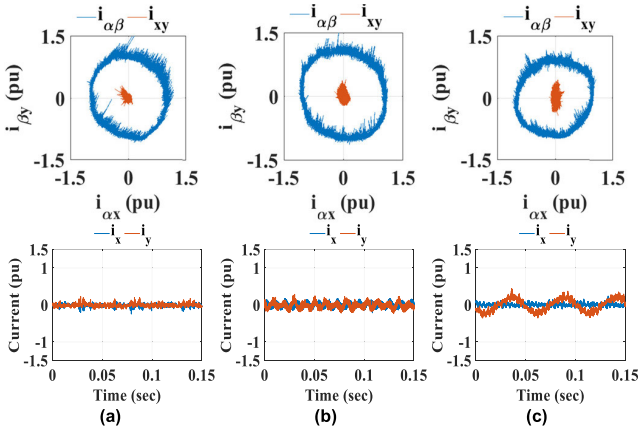

FIGURE 3. Open loop current response in $\alpha\beta$ and xy subspaces. (a) D3P (b) A6P. (c) S6P.

C. EFFECT OF MACHINE INVERTER ASYMMETRY ON THE SEQUENCE CURRENT COMPONENTS UNDER OPEN-LOOP CONTROL

One of the related points that should be highlighted in the same context is the effect of inevitable machine/converter asymmetries on the induced circulating xy current components. Theoretically, the corresponding xy current components should also be zero under sinusoidal stator excitation. However, the experimental results show an increasing xy current components at fundamental frequency and/or even order harmonics as the spatial phase angle, δ, between the two winding sets increases, being the worst under the S6P case, as shown in Fig. 3. The obtained experimental results prove that even though the reference xy sequence voltage components of the inverter output are theoretically zero, a notable xy current component can still be introduced due to winding asymmetry. This problem has been commonly solved in literature based on classical xy current control for asymmetry compensation by controlling the reference xy current component to zero [21]. However, in PCC, this problem is solved by the proper selection of applied VVs as well as the weighting factor design, as will be shown in the subsequent sections.

III. PCC OF SIX-PHASE IM

Conceptually, model predictive control (MPC) predicts the future values of the controlled variables based on system model. A predefined cost function is then used to determine the control commands that convene the control objectives to minimize the deviation between the predicted and reference variables. In predictive current control (PCC), the cost function is commonly defined as the squared error between the reference and the predicted currents for a certain voltage vector. The general block diagram of the PCC algorithm is depicted in Fig. 4. This section investigates the implantation of PCC for the three different winding configurations. In addition, it discusses the admissible voltage vectors and the need for weighting factor design for different winding configurations. PCC algorithm implementation comprises three major stages, namely, estimation, sub-spaces currents prediction, and cost function minimization, which are briefly explained in the following subsections.

A. ESTIMATION

Since the rotor variables could hardly be measured, they can simply be estimated either by lumping all non-measurable quantities and using the last values of the measured states to update this lumped value [26], or by using observers for estimating these variables [39]. In this study, the former method that incudes rotor dynamics is simply adopted without losing the concept of generalization. From (2) and using Euler discretization method, the stator flux can be estimated as follows,

$$\psi_s^{k+1} = \psi_s^k + T_s(V_{\alpha\beta}^k - R_s i_{\alpha\beta}^k) \tag{10}$$

While using (5), the rotor flux is estimated from (11).

$$\psi_r^k = \frac{L_r}{L_m}\psi_s^k + i_{s-\alpha\beta}^k \frac{L_m^2 - L_r L_s}{L_m} \tag{11}$$

where, T_s represents the sampling period.

B. PREDICTION STEP

The $\alpha\beta$ subspace currents could be predicted from stator and rotor equivalent dynamic equations by making use of the estimation step given by (10), (11) and the measured stator voltage and current as given by (12).

$$I_{\alpha\beta}^{K+1} = \left(1 + \frac{T_s}{\tau_\sigma}\right) I_{\alpha\beta}^k + \frac{T_s}{\tau_\sigma + T_s}\frac{1}{R_\sigma} \times \left\{\left(\frac{k_r}{\tau_r} - jk_r\omega\right)\psi_r^k + V_{\alpha\beta}^k\right\} \tag{12}$$

where, $R_\sigma = R_s + R_r.k_r^2$, $k_r = \frac{L_m}{L_r}$, $\tau_\sigma = \frac{\left(1-\frac{L_m^2}{L_s L_r}\right).L_s}{R_\sigma}$, and $\tau_r = \frac{L_r}{R_r}$.

While, the xy current can be predicted by discretizing (6), as given by (13).

$$I_{xy}^{K+1} = \left(1 - \frac{R_s T_s}{L_{ls}^{xy}}\right) I_{xy}^K + \frac{T_s}{L_{ls}^{xy}}(V_{xy}(i)) \tag{13}$$

Based on (13), the prediction of the xy current components will highly be affected by the leakage inductance, L_{ls}^{xy}, of this subspace, which is highly dependent on the winding configuration, as proved in [13].

C. OPTIMIZATION STEP

Through this final step, the control algorithm searches among the admissible VVs of each configuration, then, it selects the one, which minimizes the cost function given by (14).

$$g(V_s^{k+1}) = \left[\left(i_\alpha^* - i_\alpha^{k+1}\right)^2 + \left(i_\beta^* - i_\beta^{k+1}\right)^2\right] + \gamma\left[\left(i_x^* - i_x^{k+1}\right)^2 + \left(i_y^* - i_y^{k+1}\right)^2\right] \tag{14}$$

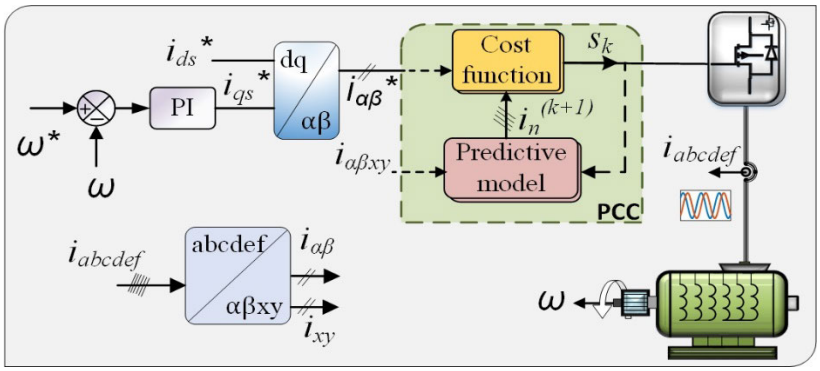

FIGURE 4. Block diagram of standard PCC of six-phase induction machine.

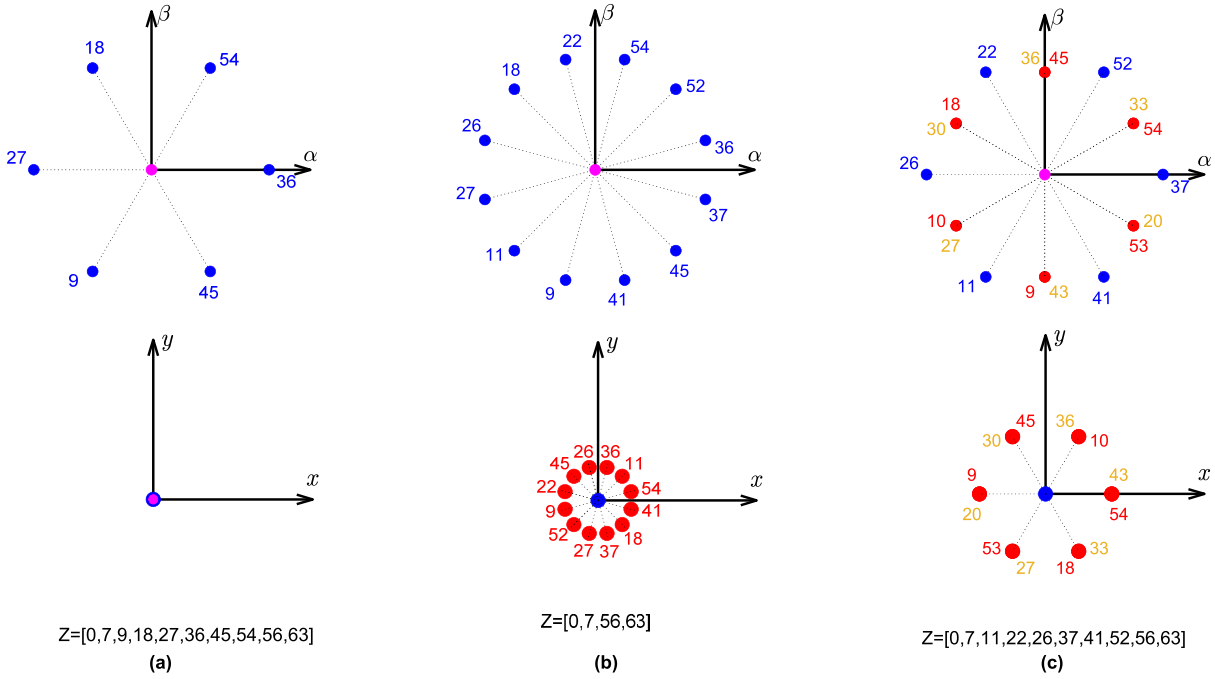

FIGURE 5. Voltage vectors mapping in both $\alpha\beta$ subspace (upper figures), and xy subspace (lower figures) for different winding configuration. (a) D3P. (b) A6P. (c) S6P.

The reference $\alpha\beta$ currents are generated based on the flux and torque requirements. Whereas, the reference xy currents are set to zero under healthy conditions. The constant γ represents the weighting factor, where its value decides the relative priority of the xy current minimization compared to the current reference tracking of the fundamental $\alpha\beta$ subspace. The optimal VV is, then, selected based on (15) and applied to the six-phase inverter in the next control sample.

$$V_s^{opt} = arg \min_{\{v_0,\ldots,v_n\}} g(V_s^{k+1}) \tag{15}$$

where, $\{v_0$ *to* $v_n\}$ are the feasible voltage vector set for each winding configuration, as will be explained in details in the following sub-section.

D. FEASIBLE VOLTAGE VECTORS

As mentioned previously, each winding configuration has its own VSD matrix, which entirely depends on the spatial phase angle between the two-winding sets. The conventional method of evaluating all distinct VVs results in a relatively high computational burden. By investigating these VVs, it is possible to reduce the number of feasible VVs that will be evaluated in each control cycle [26].

In case of D3P configuration, by referring to Tables 1 and 2, the six large VVs correspond to zero VVs in the xy plane, as shown in Fig. 5(a), which significantly reduces the xy currents in cases they have only been used. Thus, the term representing the effect of xy currents in the PCC cost function has nothing to do with the selection of the optimal voltage vectors. Therefore, this term can simply

be omitted from (14). Hence, the control algorithm is much simplified since the optimal vector is selected among only six large vectors in addition to one zero vector at each sample.

In case of A6P, it can be observed that the large vectors (L) in the $\alpha\beta$ subspace corresponds to small vectors (S) with minimum magnitude in the xy subspace, as illustrated in Fig. 5(b). Therefore, in order to achieve the best DC-link utilization with minimum xy harmonics, the large vector set will be considered only in the PCC cost function for the A6P in addition to one zero VV. This results in 13 VVs to be evaluated during each sample time.

For the S6P configuration, the six large voltage vectors in $\alpha\beta$ subspace are projected as zero voltage vectors in the xy subspace. From the first glance, large voltage vectors only seem to be the optimal vector set to be evaluated during the optimization stage of the PCC, which is the same as the D3P case. This theoretical assumption, however, yields a notable distortion due to machine/converter asymmetries, as proved by the experimental validation given in section II.C. The experimental results also showed a notable xy even order harmonic current component in case of S6P when large voltages are only recruited despite of their zero xy voltage magnitude, as will be shown later. One of the solutions proposed herein to compensate for this circulating current component is to extend the optimal voltage vector set with extra VVs having nonzero xy voltage components. This can be carried out by considering a set of medium voltage vectors with the six large VV. Taking into account that medium voltage vectors have redundant pairs in $\alpha\beta$ subspace, the selected set of the medium voltage vectors should fully span the whole xy subspace. Therefore, any of the following two medium VV groups can either be utilized: $g_1 = \{9, 10, 18, 45, 54, 53\}$ or $g_2 = \{43, 27, 30, 36, 33, 20\}$. Thus, a total of 13 VVs (6 L, 6 M and one zero) are also considered for the S6P configuration, as shown in Fig. 5(c). The PCC of S6P when utilizing the large, six of the medium VVs (g_1 or g_2) plus one zero VV will be denoted as enhanced S6P PCC in the following sections.

Regarding the performance of S6P with large vectors only, the theoretical analysis showed that despite the similarities between S6P and D3P, including the medium vectors in the S6P case, the number of active voltage vectors increases, while the weighing factor will still be mandatory to minimize the xy current components.

It is also notable that the D3P has the highest DC link utilization among other configurations, as given by Table 1. On the other hand, the S6P configuration will correspond to the samllest dc-link utilization due to the presence of medium vectors.

IV. EXPERIMENTAL WORK

A. HARDWARE DESCRIPTION

In order to investigate the behavior of various six-phase winding configurations (A6P, S6P and D3P), the customized 12-phase stator winding machine introduced in [13] has also been utilized in this study. By reconnecting multiple phases of the 12-phase machine in a specific manner, the desired six-phases winding arrangement can directly be obtained. The details of the winding layouts and the connection diagram for each configuration can be found in [13]. The ratings of the resulting six-phase machine are listed in Table 3, which are the same for all configurations. The machine equivalent circuit parameters are also estimated based on the analysis given in [13] and are summarized in Table 4 for the three winding configurations. A separately excited dc-generator is coupled to the SPIM acting as a mechanical load. The employed six-phase power inverter is constructed using two 600 V, 20 A IRAMY20UP60B three-phase inverter modules and are connected to the same DC-link. The DC-link is obtained using a 300 V programmable dc-supply. A TMS320F28379D DSP board is used in the experimental setup. Six hall-effect (LEM) current sensors are used to measure phase currents, and a hole effect speed sensor is used for speed measurement. The whole experimental setup is illustrated in Fig. 6.

TABLE 3. Prototype machine specifications.

Rated RMS phase Voltage (V)	110
Rated Power (kW)	1
Rated RMS phase current (A)	2.8
Rated frequency (Hz)	50
No. of poles	4
Rated speed (RPM)	1400

TABLE 4. Prototype machine sequence parameters under different connections.

Parameter	D3P	S6P	A6P
R_s	4.18 Ω	4.18 Ω	4.18 Ω
R_r	3.46 Ω	3.46 Ω	3.67 Ω
$L_{ls}^{\alpha\beta}$	9.1 mH	9.1 mH	12 mH
$L_{lr}^{\alpha\beta}$	19.1 mH	19.1 mH	16.7 mH
$L_{m}^{\alpha\beta}$	254 mH	260 mH	247 mH
L_{ls}^{xy}	11.8 mH	11.8 mH	7.5 mH
γ	N/A	0.1	0.3

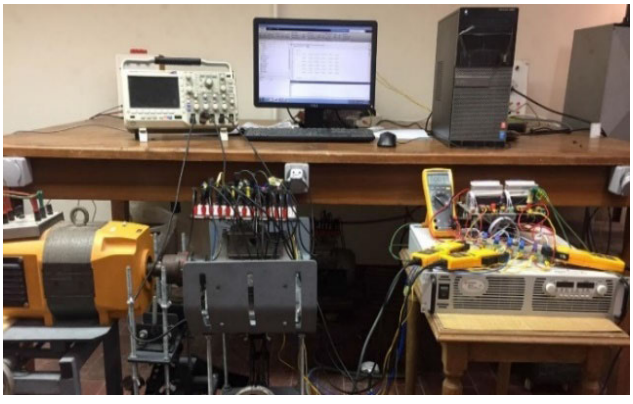

FIGURE 6. Experimental six-phase setup.

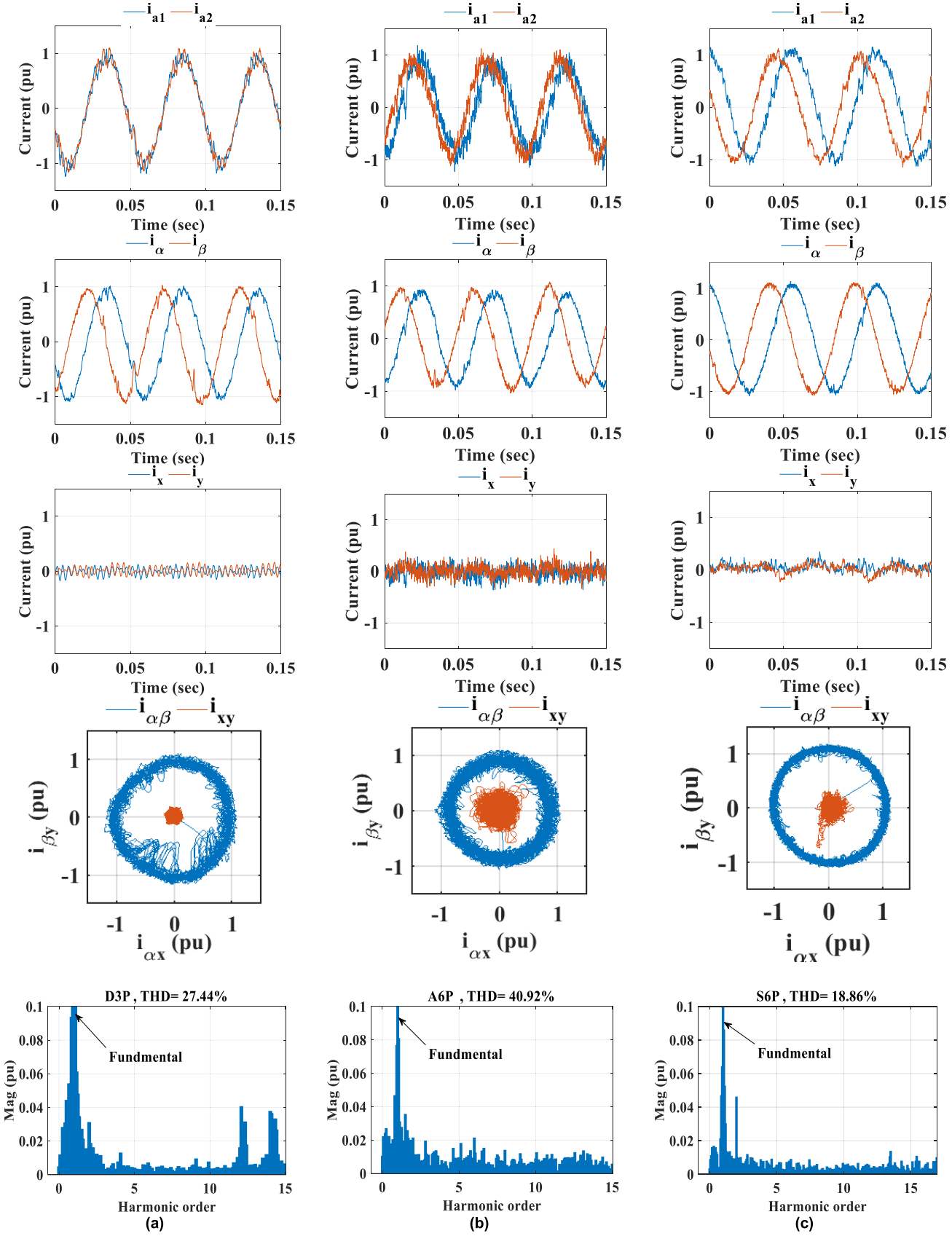

FIGURE 7. Measured current waveforms for PCC in per unit at 500 RPM. (a) D3P(6L+Z VVs). (b) A6P(12L+Z VVs) (c) Enhanced S6P (6L+6M+Z VVs).

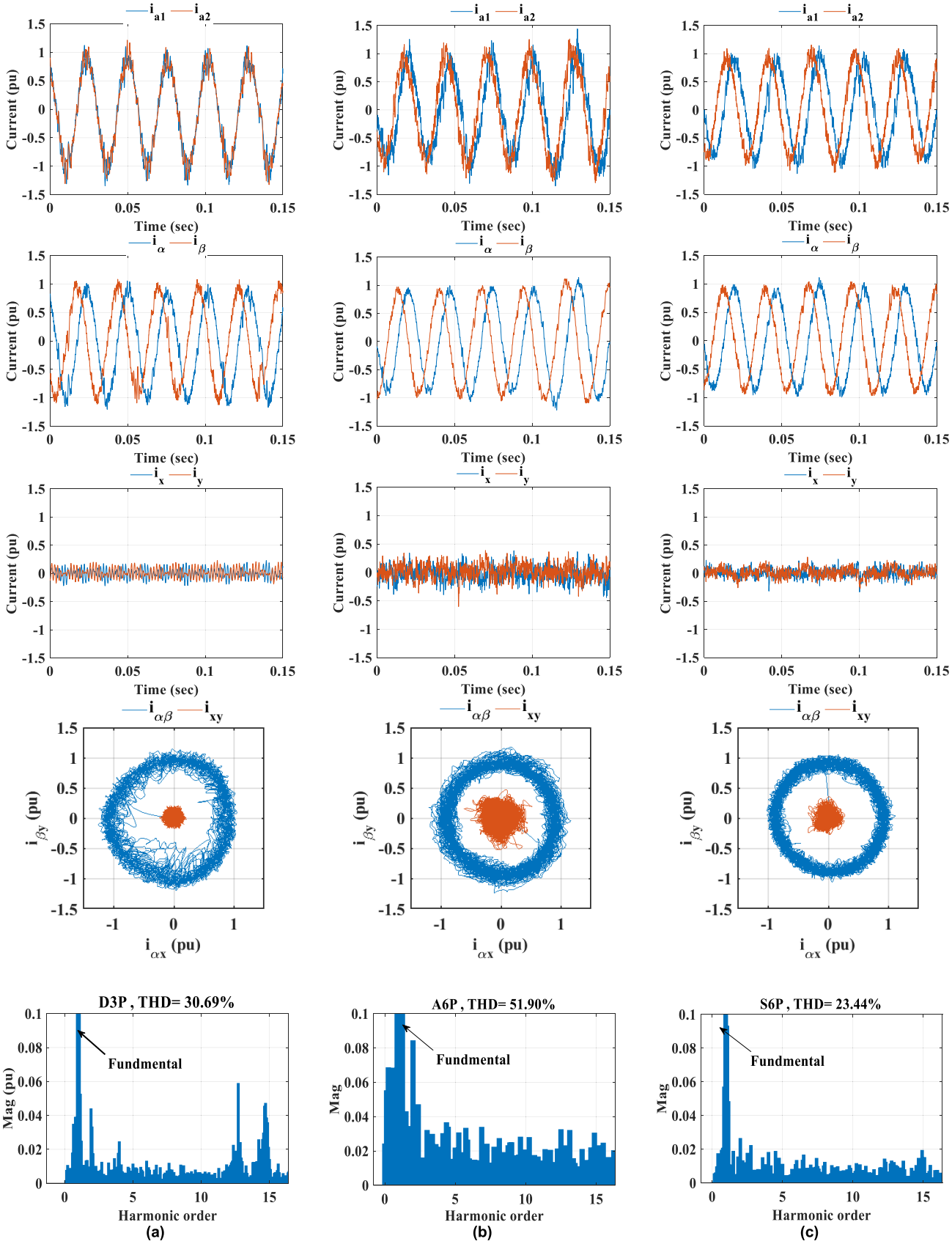

FIGURE 8. Measured current waveforms for PCC in per unit at 1000 RPM. (a) D3P(6L+Z VVs). (b) A6P(12L+Z VVs). (c) Enhanced S6P (6L+6M+Z VVs).

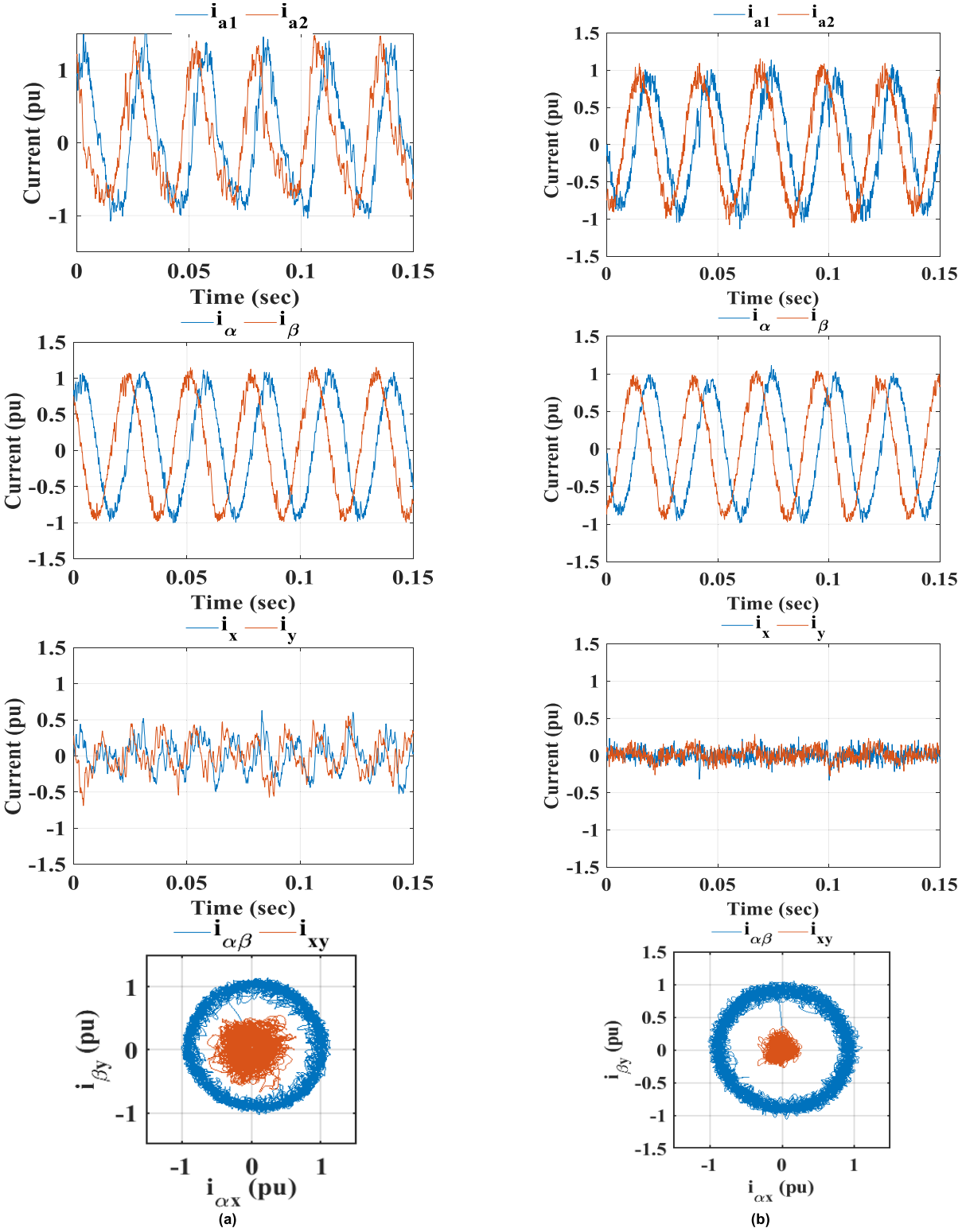

FIGURE 9. Comparison between S6P current waveforms at 1000RPM using (a) S6P(6L+Z VVs) and (b) enhanced S6P (6L+6M+Z VVs).

In the following, various tests are carried out to assess the effect of winding configuration of the SPIM using PCC technique under both dynamic and steady state conditions. All experiments have been carried out at rated torque, d-current reference of 2A, sampling time of 50 μ sec, and 500 RPM reference speed.

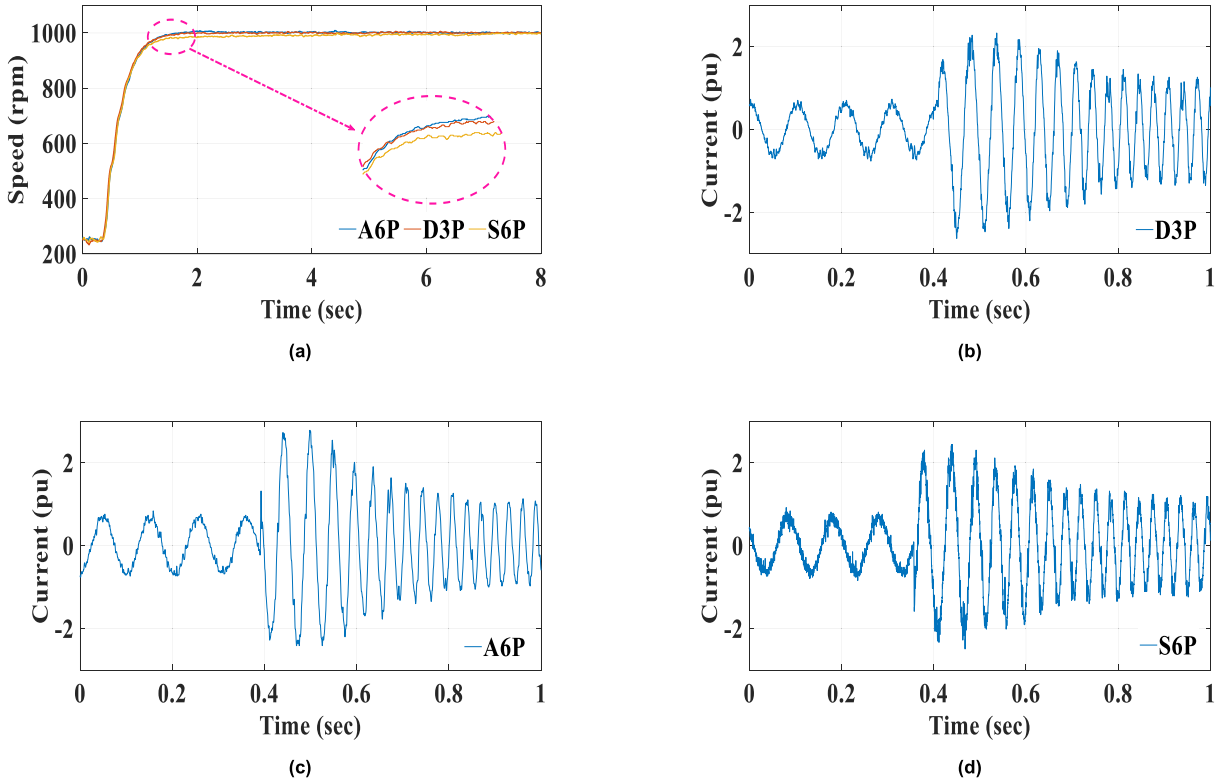

FIGURE 10. Measured speed and current dynamic response of different winding configuration. (a) Speed response for D3P, A6P, and Enhanced S6P. Phase current response for (b) D3P, (c) A6P, and (d) Enhanced S6P.

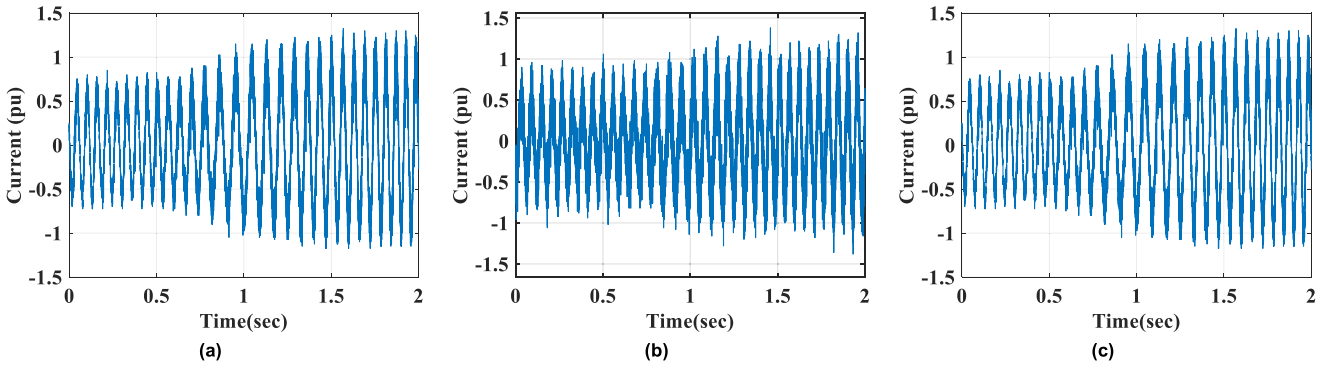

FIGURE 11. Sudden loading phase current response of different winding configuration. a) D3P. b) A6P. c) Enhanced S6P.

Based on the analysis made in the previous section, best dc-link utilization with less time consuming is achieved by considering large vectors only for the D3P and A6P configurations. Whereas, improving the current waveform of S6P connection entails the inclusion of medium vectors in the optimization problem. The weighting factor, γ, for each configuration is obtained based on trial and error and is given in Table 4. As previously mentioned, the operation of D3P does not entail a weighting factor since neither the applied large vector nor possible machine asymmetries result in notable *xy* current components, as indicated by the open loop response and as will be shown in the following results.

B. STEADY STATE OPERATION

Figs. 7 and 8 compare the steady-state phase currents corresponding to the three configurations at low speed (500 RPM) and high speed (1000 RPM) values, respectively. Figs. 8(a) and 9(a) show that the D3P phase current has small current ripples and minimum *xy* current components. This is a result of evaluating the large vectors only, which are mapped

into zero vectors in the *xy* subspace as well as the relatively high inductance of the *xy* subspace of this configuration [13]. However, it is worth mentioning that the employed SPIM has a notable high frequency current component in the phase current and is mapped to the $\alpha\beta$ subspace due to slot harmonics under D3P, as clear from the FFT plots given in Figs. 7 and 8. This phenomenon has been highlighted in [13] and can simply be avoided by the proper selection of the stator slot/rotor bar combination in the machine design phase.

Figs. 7(b) and 8(b) show that the A6P phase currents under the same two speeds, respectively, experience significant high current ripple due to its relatively small inductance of the secondary subspace, as listed in Table 4. In addition, the selected VVs in the case of A6P are mapped as small vectors in *xy* subspace, but not zeros as the case of D3P.

Figs. 7(c) and 8(c) illustrate the SP6 case under the proposed PCC for this connection, which corresponds to the best current tracking and best total harmonic distortion (THD). To focus on the effect of voltage vector selection on this specific connection, Fig. 9 compares two cases while the speed reference is set to 1000 rpm. Fig. 9(a) shows the S6P phase currents when large vectors are only employed. Clearly, this non optimal case results in highly distorted asymmetric phase current waveforms, which yields a significant circulating *xy* even order harmonic current component due to this notable asymmetry in the phase current. On the other hand, the current waveform for the same connection is significantly improved in Fig. 9(b) by introducing the suitable six medium VVs into PCC in order to produce a small *xy* voltage component to compensate for these secondary current components.

C. DYNAMIC RESPONSE

To compare the dynamic response of different winding configurations, a step speed response from 250 RPM to 1000 RPM is performed and the experimental results for the three cases are shown in Fig. 10. Also, the phase current responses of the three configurations under step loading with rated load torque are shown in Fig. 11. Clearly, the winding configuration has almost no effect on the dynamic response of the SPIM which mainly depends on the fundamental $\alpha\beta$ currents. It has been concluded in [13] that the effect of winding configuration on the torque production among the three connections is minimal. This may also be concluded from the $\alpha\beta$ current magnitudes under the same load torque given in Figs. 7 and 8. Albeit, there is a little bit difference in case of the enhanced PCC for S6P case since the dc-link utilization is slightly reduced as a result of including medium voltages.

V. CONCLUSION

This paper investigated the performance of PCC applied to SPIM with different winding configurations, namely, D3P, A6P, and S6P. The relevant literature improved the performance of SPIM based MPC by employing more complex, and time-consuming control techniques. This paper, however, showed that employing a proper winding configuration may be a simple and a more efficient option to improve the performance of conventional PCC while greatly simplifying the VV selection as well as the control computational burden. It has been shown that each winding configuration results in different voltage vector sets mapped to both $\alpha\beta$ and *xy* with different amplitudes. Considering only large vectors, the experiments showed that the behavior of the $\alpha\beta$ subspace may be assumed the same for all configurations. However, the *xy* current component differed greatly among the three cases. PCC of A6P results in a relatively poor current waveform, which adds no new conclusions over the available literature. The most salient conclusion of this study is the effect of winding configuration on the induced *xy* current components due to winding asymmetry. It has been concluded that the effect of winding asymmetry pronounces more as the spatial phase angle between the two three-phase sets increases, being the worst under S6P configuration. Although the voltage vector mapping for the D3P and S6P looks pretty the same, the latter connection showed a notable asymmetry in the phase current waveform and a significant *xy* current component. This problem has simply been compensated for by including the medium vectors in the PCC optimization process of the S6P connection at the cost of a reduced dc-link utilization. However, it yields the best current tracking and THD in the phase current among the three connections. On the other hand, the study showed that the D3P corresponds to an improved current waveform over A6P connection, minimum number of voltage vector, elimination of weighting factor, and minimum computational burden.

REFERENCES

[1] A. Salem and M. Narimani, "A review on multiphase drives for automotive traction applications," *IEEE Trans. Transport. Electrific.*, vol. 5, no. 4, pp. 1329–1348, Dec. 2019.

[2] E. Levi, F. Barrero, and M. J. Duran, "Multiphase machines and drives—Revisited," *IEEE Trans. Ind. Electron.*, vol. 63, no. 1, pp. 429–432, Jan. 2016.

[3] F. Barrero and M. J. Duran, "Recent advances in the design, modeling, and control of multiphase machines—Part I," *IEEE Trans. Ind. Electron.*, vol. 63, no. 1, pp. 449–458, Jan. 2016.

[4] M. J. Duran and F. Barrero, "Recent advances in the design, modeling, and control of multiphase machines—Part II," *IEEE Trans. Ind. Electron.*, vol. 63, no. 1, pp. 459–468, Jan. 2016.

[5] H. S. Che, A. S. Abdel-Khalik, O. Dordevic, and E. Levi, "Parameter estimation of asymmetrical six-phase induction machines using modified standard tests," *IEEE Trans. Ind. Electron.*, vol. 64, no. 8, pp. 6075–6085, Aug. 2017.

[6] T. Tao, W. Zhao, Y. Du, Y. Cheng, and J. Zhu, "Simplified fault-tolerant model predictive control for a five-phase permanent-magnet motor with reduced computation burden," *IEEE Trans. Power Electron.*, vol. 35, no. 4, pp. 3850–3858, Apr. 2020.

[7] I. Gonzalez-Prieto, M. J. Duran, M. Bermudez, F. Barrero, and C. Martin, "Assessment of virtual-voltage-based model predictive controllers in six-phase drives under open-phase faults," *IEEE J. Emerg. Sel. Topics Power Electron.*, vol. 8, no. 3, pp. 2634–2644, Sep. 2020.

[8] M. Y. Metwly, M. S. Abdel-Majeed, A. S. Abdel-Khalik, R. A. Hamdy, M. S. Hamad, and S. Ahmed, "A review of integrated on-board EV battery chargers: Advanced topologies, recent developments and optimal selection of FSCW slot/pole combination," *IEEE Access*, vol. 8, pp. 85216–85242, 2020.

[9] E. Levi, "Advances in converter control and innovative exploitation of additional degrees of freedom for multiphase machines," *IEEE Trans. Ind. Electron.*, vol. 63, no. 1, pp. 433–448, Jan. 2016.

[10] E. Jung, H. Yoo, S.-K. Sul, H.-S. Choi, and Y.-Y. Choi, "A nine-phase permanent-magnet motor drive system for an ultrahigh-speed elevator," *IEEE Trans. Ind. Appl.*, vol. 48, no. 3, pp. 987–995, May 2012.

[11] A. Shawier, A. S. Abdel-Khalik, R. A. Hamdy, K. H. Ahmed, and S. Ahmed, "Postfault operation of five-phase induction machine with minimum total losses under single open-phase fault," *IEEE Access*, vol. 8, pp. 208696–208706, 2020.

[12] J. P. Puente, B. Prieto, M. Satrustegui, I. Elosegui, and P. Gonzalez, "Improving the performance of a 1 MW induction machine by optimally shifting from a 3-phase to a 6-phase machine design by rearranging the coil connections," *IEEE Trans. Ind. Electron.*, vol. 68, no. 2, pp. 1035–1045, Feb. 2021.

[13] A. S. Abdel-Khalik, M. S. Abdel-Majeed, and S. Ahmed, "Effect of winding configuration on six-phase induction machine parameters and performance," *IEEE Access*, vol. 8, pp. 223009–223020, 2020.

[14] W. N. W. A. Munim, M. J. Duran, H. S. Che, M. Bermudez, I. Gonzalez-Prieto, and N. A. Rahim, "A unified analysis of the fault tolerance capability in six-phase induction motor drives," *IEEE Trans. Power Electron.*, vol. 32, no. 10, pp. 7824–7836, Oct. 2017.

[15] E. Levi, R. Bojoi, F. Profumo, H. Toliyat, and S. Williamson, "Multiphase induction motor drives-a technology status review," *IET Electr. Power Appl.*, vol. 1, no. 4, pp. 489–516, 2007.

[16] R. O. C. Lyra and T. A. Lipo, "Torque density improvement in a six-phase induction motor with third harmonic current injection," *IEEE Trans. Ind. Appl.*, vol. 38, no. 5, pp. 1351–1360, Sep. 2002.

[17] G. K. Singh, V. Pant, and Y. P. Singh, "Voltage source inverter driven multi-phase induction machine," *Comput. Electr. Eng.*, vol. 29, no. 8, pp. 813–834, Nov. 2003.

[18] H. Razik, A. Rezzoug, and D. Hadiouche, "Modelling and analysis of dual-stator induction motors," *IEEJ Trans. Ind. Appl.*, vol. 125, no. 12, pp. 1093–1104, 2005.

[19] Y. Zhao and T. A. Lipo, "Space vector PWM control of dual three-phase induction machine using vector space decomposition," *IEEE Trans. Ind. Appl.*, vol. 31, no. 5, pp. 1100–1109, Sep. 1995.

[20] E. Levi, "Multiphase electric machines for variable-speed applications," *IEEE Trans. Ind. Electron.*, vol. 55, no. 5, pp. 1893–1909, May 2008.

[21] H. S. Che, E. Levi, M. Jones, W.-P. Hew, and N. A. Rahim, "Current control methods for an asymmetrical six-phase induction motor drive," *IEEE Trans. Power Electron.*, vol. 29, no. 1, pp. 407–417, Jan. 2014.

[22] D. Hadiouche, L. Baghli, and A. Rezzoug, "Space-vector PWM techniques for dual three-phase AC machine: Analysis, performance evaluation, and DSP implementation," *IEEE Trans. Ind. Appl.*, vol. 42, no. 4, pp. 1112–1122, Jul. 2006.

[23] D. Glose and R. Kennel, "Carrier-based pulse width modulation for symmetrical six-phase drives," *IEEE Trans. Power Electron.*, vol. 30, no. 12, pp. 6873–6882, Dec. 2015.

[24] B. M. Shihab, M. Tousizadeh, and H. S. Che, "Continuous and discontinuous PWM methods for symmetrical six-phase induction motor with single isolated neutral," *Arabian J. Sci. Eng.*, vol. 45, no. 3, pp. 1885–1895, Mar. 2020.

[25] P. Karamanakos, E. Liegmann, T. Geyer, and R. Kennel, "Model predictive control of power electronic systems: Methods, results, and challenges," *IEEE Open J. Ind. Appl.*, vol. 1, pp. 95–114, 2020.

[26] F. Barrero, M. R. Arahal, R. Gregor, S. Toral, and M. J. Duran, "A proof of concept study of predictive current control for VSI-driven asymmetrical dual three-phase AC machines," *IEEE Trans. Ind. Electron.*, vol. 56, no. 6, pp. 1937–1954, Jun. 2009.

[27] F. Barrero, J. Prieto, E. Levi, R. Gregor, S. Toral, M. J. Duran, and M. Jones, "An enhanced predictive current control method for asymmetrical six-phase motor drives," *IEEE Trans. Ind. Electron.*, vol. 58, no. 8, pp. 3242–3252, Aug. 2011.

[28] J. A. Riveros, F. Barrero, E. Levi, M. J. Duran, S. Toral, and M. Jones, "Variable-speed five-phase induction motor drive based on predictive torque control," *IEEE Trans. Ind. Electron.*, vol. 60, no. 8, pp. 2957–2968, Aug. 2013.

[29] M. J. Duran, J. Prieto, F. Barrero, and S. Toral, "Predictive current control of dual three-phase drives using restrained search techniques," *IEEE Trans. Ind. Electron.*, vol. 58, no. 8, pp. 3253–3263, Aug. 2011.

[30] S. Vazquez, J. Rodriguez, M. Rivera, L. G. Franquelo, and M. Norambuena, "Model predictive control for power converters and drives: Advances and trends," *IEEE Trans. Ind. Electron.*, vol. 64, no. 2, pp. 935–947, Feb. 2017.

[31] M. R. Arahal, C. Martín, A. Kowal, M. Castilla, and F. Barrero, "Cost function optimization for predictive control of a five-phase IM drive," *Optim. Control Appl. Methods*, vol. 41, no. 1, pp. 84–93, Jan. 2020.

[32] M. Mamdouh and M. A. Abido, "Weighting factor elimination for predictive current control of asymmetric six phase induction motor," in *Proc. IEEE Int. Conf. Environ. Electr. Eng. IEEE Ind. Commercial Power Syst. Eur. (EEEIC / I&CPS Eur.)*, Jun. 2020, pp. 1–6.

[33] I. Gonzalez-Prieto, M. J. Duran, J. J. Aciego, C. Martin, and F. Barrero, "Model predictive control of six-phase induction motor drives using virtual voltage vectors," *IEEE Trans. Ind. Electron.*, vol. 65, no. 1, pp. 27–37, Jan. 2018.

[34] Y. Luo and C. Liu, "A flux constrained predictive control for a six-phase PMSM motor with lower complexity," *IEEE Trans. Ind. Electron.*, vol. 66, no. 7, pp. 5081–5093, Jul. 2019.

[35] C. Xue, W. Song, X. Wu, and X. Feng, "A constant switching frequency finite-control-set predictive current control scheme of a five-phase inverter with duty-ratio optimization," *IEEE Trans. Power Electron.*, vol. 33, no. 4, pp. 3583–3594, Apr. 2018.

[36] A. S. Abdel-Khalik, A. M. Massoud, and S. Ahmed, "Nine-phase six-terminal induction machine modeling using vector space decomposition," *IEEE Trans. Ind. Electron.*, vol. 66, no. 2, pp. 988–1000, Feb. 2019.

[37] A. S. Abdel-Khalik, A. M. Massoud, and S. Ahmed, "An improved torque density pseudo six-phase induction machine using a quadruple three-phase stator winding," *IEEE Trans. Ind. Electron.*, vol. 67, no. 3, pp. 1855–1866, Mar. 2020.

[38] S. Sharma, M. V. Aware, and A. Bhowate, "Symmetrical six-phase induction motor-based integrated driveline of electric vehicle with predictive control," *IEEE Trans. Transport. Electrific.*, vol. 6, no. 2, pp. 635–646, Jun. 2020.

[39] C. Martin, M. R. Arahal, F. Barrero, and M. J. Duran, "Five-phase induction motor rotor current observer for finite control set model predictive control of stator current," *IEEE Trans. Ind. Electron.*, vol. 63, no. 7, pp. 4527–4538, Jul. 2016.

ABDULLAH SHAWIER received the B.Sc. degree in electrical engineering from Alexandria University, Alexandria, Egypt, in 2016. He is currently a Demonstrator with the Department of Electrical Engineering, Faculty of Engineering, Alexandria University. His current research interests include electric drives, battery chargers, electric vehicles, and renewable energy systems.

ABDELRAHMAN HABIB received the B.Sc. degree in electrical engineering from Alexandria University, Alexandria, Egypt, in 2018. He is currently a Demonstrator with the Department of Electrical Engineering, Faculty of Engineering, Alexandria University. His current research interests include electric drives, battery chargers, electric vehicles, embedded systems, and solid-state power conversion.

MOHAMED MAMDOUH received the B.Sc. degree (Hons.) in electrical power and machines from the Faculty of Engineering, Tanta University, Egypt, in 2007, the M.Sc. degree in mechatronics and robotics from the Egypt-Japan University of Science and Technology (E-JUST), Egypt, in 2012, and the Ph.D. degree in electrical engineering from the King Fahd University of Petroleum and Minerals (KFUPM), in 2018. He currently works as an Assistant Professor with the Department of Electrical Power and Machines, Faculty of Engineering, Tanta University. His current research interest includes model predictive control of electric drive systems.

AYMAN SAMY ABDEL-KHALIK (Senior Member, IEEE) received the B.Sc. and M.Sc. degrees in electrical engineering from Alexandria University, Alexandria, Egypt, in 2001 and 2004, respectively, and the Ph.D. degree in electrical engineering from Alexandria University, and University of Strathclyde, Glasgow, U.K., in 2009, under a dual channel program. He is currently a Professor with the Department of Electrical Engineering, Faculty of Engineering, Alexandria University. His current research interests include electrical machine design and modelling, electric drives, energy conversion, and renewable energy. He serves as an Associate Editor for IEEE TRANSACTIONS ON INDUSTRIAL ELECTRONICS and *IET Electric Power Applications* Journal. He also serves as the Executive Editor for *Alexandria Engineering Journal*.

KHALED H. AHMED (Senior Member, IEEE) received the B.Sc. (Hons.) and M.Sc. degrees from Alexandria University, Egypt, in 2002 and 2004, respectively, and the Ph.D. degree in power electronics applications from the University of Strathclyde, U.K., in 2008. He has been appointed as a Professor with Alexandria University, since 2019. He is currently a Reader in power electronics with the University of Strathclyde. He has published more than 110 technical articles in refereed journals and papers in conferences. He has published a textbook entitled *High Voltage Direct Current Transmission: Converters, Systems and DC Grids*, a book chapter contribution, and a PCT patent PCT/GB2017/051364. His research interests include renewable energy integration, high power converters, offshore wind energy, DC/DC converters, HVDC, and smart grids. He is a Senior Member of IEEE Power Electronics and Industrial Electronics Society.